Article

Effect of Graphene Oxide and Fly Ash on Frost Resistance of the Steel Fiber Reinforced Concrete

Xiaosa Yuan *, Mingjiang Dai, Mengfan Li, Shanshan Zhang and Mingming Zhang

Shaanxi Key Laboratory of Safety and Durability of Concrete Structures, Xijing University, Xi'an 710123, China; 15387859640@163.com (M.D.); limengfan821@163.com (M.L.); zhangshanshan39@163.com (S.Z.); mingzai86782021@163.com (M.Z.)
* Correspondence: yuanxiaosa2009@163.com; Tel.: +86-18710543299

Abstract: The addition of graphene oxide (GO) and fly ash (FA) to SFRC (steel fiber reinforced concrete) increases frost resistance. Based on the analysis of the amelioration of GO on the frost resistance of SFRC, the improvement mechanism and the effects of GO and FA on the durability of SFRC were studied in depth. The test blocks' compressive strength, relative dynamic modulus of elasticity, and mass-loss rate were tested through experiments. The pore distribution and morphological characteristics of concrete were captured by industrial CT scanning technology. The effects of GO and FA on the pore distribution and morphology of the SFRC are discussed. The results show that the compressive strength of GO-SFRC(graphene oxide and steel fiber reinforced concrete)with GO proportion of 0.03% is 28.20% higher than that of ordinary SFRC without freezing and thawing; after 100 freeze-thaw cycles, the compressive strength of the $G_{0.03}S_{25}$ increased by 31.70% compared with the compressive strength of the $G_{0.00}S_{25}$, and pore shape of $G_{0.03}S_{25}$ presents a spherical shape and an elliptical spherical shape; based on the data analysis of the strength loss, relative dynamic elastic modulus loss and mass-loss rate, it is considered that the properties of ordinary SFRC are the worst under freezing and thawing; as FA admixture increases, the porosity decreases; with FA of 30% and GO of 0.03%, the GO-FA-SFRC has the best frost resistance, as well as most of the pores are closed which resemble spheres and ellipsoids.

Keywords: frost resistance; graphene oxide; fly ash; synergistic effect; steel fiber reinforced concrete

1. Introduction

In the low-temperature environment, the water molecules in the micropores of concrete are subject to the alternating action of positive and negative temperatures. The periodic change of volume expansion-contraction will occur and eventually lead to the tensile stress in the micropores. The long-term effect of tensile stress will make the concrete crack, surface slurry spalling, exposed aggregate, and destroy its strength and durability. Therefore, frost resistance is a significant index in the design of concrete structures in cold regions. The fundamental way to improve the durability of concrete structures is to increase compactness.

In recent years, the application of nanotechnology has become more and more popular in different scientific fields [1,2]. Typical nanomaterials include SiO_2, TiO_2, Nano-Fe_2O_3, nano-Al_2O_3, carbon nanotubes/fibers, and graphene oxide nanosheets [3]. Many studies have proved that the addition of nanomaterials can improve cement-based compressive strength and enhance permeability [4–12]. GO is the oxidation reaction product of graphene, a mixture of functional groups with single sp^2 hybrid carbon, carboxyl, epoxy, and hydroxyl. It has a high specific surface area to show better performance in the hardened state of concrete [13,14]. An appropriate amount of GO can promote the growth of hydrated crystals of cement mortar, change the size and shape of crystals, and form a stable and compact structure [15–18]. GO as a core point can improve hydration rate, enhance the amount of calcium silicate hydrate (C-S-H), reduce the crystal size of Ca $(OH)_2$, and play a

role in regulating pore structure [19–24]. It has been studied that mechanical properties can be improved by adding the appropriate amount of GO [25–29].

Fly ash is a fine mineral admixture in concrete, with primarily spherical and vitreous particles. Mixing fly ash into concrete can increase compactness [30,31]. Wu Qianyun et al. indicated that an appropriate amount of basalt fiber can improve the frost resistance of concrete [32]. GO enhanced the activity effect of fly ash cement-based materials at an early age [33]. Li Dongpo et al. found out that GO and SP could improve mechanical properties of cement-based composites after freeze-thaw cycles [34]. Combined with the characteristics of GO and FA, this paper will further study the durability of steel fiber concrete under the conditions of freeze-thaw cycles and provide a reference for related research and engineering application.

2. Materials and Methods

2.1. Material Parameters

This experiment used P·O42.5ordinary silicate cement and grade I fly ash, whose chemical composition and essential physical properties are shown in Tables 1–3, respectively. The physical properties of Shear-shaped wavy steel fibers with a size of 37 mm × 1 mm × 0.8 mm are seen in Table 4. The size of coarse aggregate with continuous grading is 4.75–19 mm, and its parameters are presented in Table 5. The fine aggregate is river sand with a fineness module of 2.61. The water-reducing agent produced by Subote New Materials Co., Ltd. (Nanjing, China) is used as an admixture, whose technical indexes are shown in Table 6.

Table 1. Chemical composition of P·O42.5 and fly ash (%).

Category	Chemical Component									
	SiO_2	Fe_2O_3	Al_2O_3	CaO	MgO	SO_3	Na_2O	K_2O	Alkali Content	Loss on Ignition
cement	21.58	3.36	5.62	61.31	2.32	2.41	0	0	0.54	2.86
FA	49.02	6.97	31.56	4.88	0.83	0	1.05	0.73	0	0

Table 2. Physical and mechanical indexes of cement.

Density (G/cm^3)	Specific Surface Area (M^2/Kg)	Fineness (%)	Setting Time (Min)		Compressive Strength (Mpa)		Breaking Strength (Mpa)	
			Initial Set	Final Set	3d	28d	3d	28d
3.10	360	3.8	125	180	24.0	50.5	4.7	8.3

Table 3. Physical properties of fly ash.

Fineness (45 μm)	Water Demand Ratio	Ignition Loss	Moisture Content	SO_3
18%	94%	3.65%	0.3%	1.2%

Table 4. Physical properties of steel fiber.

| Length (Mm)	Diameter (Mm)	Thickness (Mm)	Strength of Extension (Mpa)	Density (G/cm^3)
37	1	0.8	400	7.83

Table 5. Physical properties of coarse aggregate.

Designation	Apparent Density (Kg/cm^3)	Stacking Density (Kg/cm^3)	Water Absorption/%
coarse aggregate	2840	1730	0.55

Table 6. Technical indexes of water reducing agent.

Appearance	Hydroxyl (-Oh)	Ph	Moisture	Solubility
Pale yellow to white flaky	22~27	5.0~7.0	≤0.5	Soluble in water and a variety of organic matter

GO is the product of graphene oxidation reaction, which contains many carboxyl, hydroxyl, and oxygen-containing bases. GO is commonly used in the study of concrete because of the larger surface area, strong interface force and good dispersion in water. The GO was produced by Suzhou Carbonfeng Graphene Technology Co., Ltd. (Suzhou, China). In addition, the dispersion degree of GO aqueous solution is measured by scanning, as shown in Figure 1, and the main parameters are shown in Tables 7 and 8.
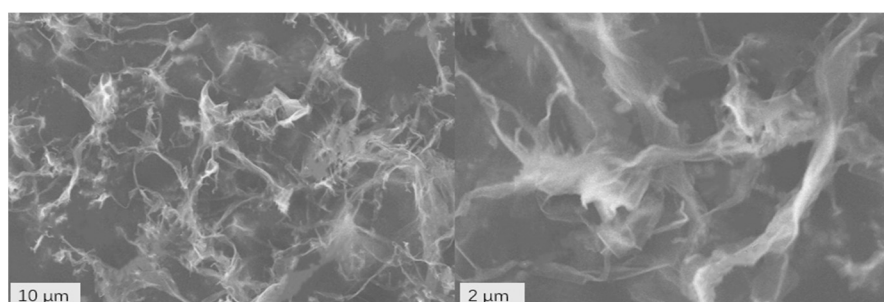
Figure 1. Dispersion degree of the GO aqueous solution.

Table 7. Parameters of GO dispersion aqueous solution.

Purity (Wt%)	Thickness (Nm)	Diameter Lamella (Nm)	The Layer Number	Specific Surface Area (M^2/G)	Appearance
>95	3.4–7	10–50	6–10	100–300	Dark brown

Table 8. Proportion of GO elements.

Components	Area (CPS)	Contents
C	23,326.9	68.44%
O	27,825.9	30.92%
S	467.1	0.63%

2.2. Test Design

This experiment investigated the effect of GO and FA on the durability of SFRC under freeze-thaw cycles. The quality ratio of GO to fine aggregate was 0.01%, 0.03%, 0.05%, and 0.07%, respectively. The content of GO is 65.265 g/m^3, 195.795 g/m^3, 326.325 g/m^3 and 456.855 g/m^3, respectively. The content of fly ash replacing cement was 15%, 30%, and 45%, respectively. The fixed dosage of steel fiber was 25 kg/m^3. Cubic test blocks with dimensions of 100 mm × 100 mm × 100 mm were used. After pouring and vibrating, the specimens were de-molded at 24 h and then placed in the standard curing box (Figure 2) for 28 days. The mixed proportions of specimens are shown in Table 9.

Figure 2. The standard curing box.

Table 9. Mix proportions of specimens (kg/m^3).

Specimen Number	Cement	Grit	Stone	Water	GO	FA	Steel Fiber	Water Reducer
$G_{0.00}S_{25}$	456	687	1030.5	164	0	0	25	2
$G_{0.01}S_{25}$	456	687	1030.5	157.13	0.0687	0	25	2
$G_{0.03}S_{25}$	456	687	1030.5	143.39	0.2061	0	25	2
$G_{0.05}S_{25}$	456	687	1030.5	129.65	0.3435	0	25	2
$G_{0.07}S_{25}$	456	687	1030.5	115.91	0.4809	0	25	2
$G_{0.01}F_{15}S_{25}$	387.4	687	1030.5	157.13	0.0687	68.4	25	2
$G_{0.03}F_{15}S_{25}$	387.4	687	1030.5	143.39	0.2061	68.4	25	2
$G_{0.05}F_{15}S_{25}$	387.4	687	1030.5	129.65	0.3435	68.4	25	2
$G_{0.07}F_{15}S_{25}$	387.4	687	1030.5	115.91	0.4809	68.4	25	2
$G_{0.01}F_{30}S_{25}$	319.2	687	1030.5	157.13	0.0687	136.8	25	2
$G_{0.03}F_{30}S_{25}$	319.2	687	1030.5	143.39	0.2061	136.8	25	2
$G_{0.05}F_{30}S_{25}$	319.2	687	1030.5	129.65	0.3435	136.8	25	2
$G_{0.07}F_{30}S_{25}$	319.2	687	1030.5	115.91	0.4809	136.8	25	2
$G_{0.01}F_{45}S_{25}$	250.8	687	1030.5	115.91	0.0687	205.2	25	2
$G_{0.03}F_{45}S_{25}$	250.8	687	1030.5	115.91	0.2061	205.2	25	2
$G_{0.05}F_{45}S_{25}$	250.8	687	1030.5	115.91	0.3435	205.2	25	2
$G_{0.07}F_{45}S_{25}$	250.8	687	1030.5	115.91	0.4809	205.2	25	2

Note: $G_{0.01}F_{15}S_{25}$ represents 0.01% of GO's content, fly ash replacement rate is 15%, and steel fiber content is 25%.

2.3. Experiment Method

2.3.1. Freeze-Thaw Cycle Test

According to GB-T50082-2009, the specimens were soaked in clean water for 96 h, wiped off the surface moisture and then put into the rapid freeze-thaw testing machine (Figure 3a), with being set to freeze for 6 h at a cycle. The equipment is produced by Tianjin Gangyuan Test Instrument Co., Ltd. (Wenzhou, China). Five freeze-thaw cycle conditions were considered, i.e., 0, 25, 50, 75, and 100 freeze-thaw cycles. During the test, the temperature of the specimen center should be controlled from (-18 ± 2) °C to (5 ± 2) °C.

The mass loss, relative dynamic modulus of elasticity (measured by the equipment, seen in Figure 3b, and compressive strength loss were carried out to evaluate the frost resistance of concrete. The equipment was produced by Tianjin Gangyuan Test Instrument Co., Ltd. (Wenzhou, China). To assess the mass loss, the spalling amount per unit area, M_n, is

$$M_n = \frac{m_n}{S} \tag{1}$$

where m_n is accumulated dry flaking mass after 'n' freeze-thaw cycles and S is the surface area of contact solution.

(**a**)	(**b**)

Figure 3. Test Instruments: (**a**) Concrete rapid freeze-thaw testing machine; (**b**) Concrete dynamic elastic modulus tester.

2.3.2. Industrial CT Scanning

Multiscale-Voxel 450 produced by Sanying Precision Instruments Co., Ltd. (Tianjin, China) was used for scanning concrete specimens. Avizo software was used for the post-processing of CT data to explore the internal pore structure. In order to reduce errors caused by boundaries and obtain accurate and effective in-situ CT data, a square slice with the dimensions of 90 mm $\times$ 90 mm was taken as the research object without damaging the original internal structure. Before DR Film was taken for correction, the voltage was set to 385 kV and the current to 1.3 mA. A correction scan was performed before each CT scan, and the same parameters were selected for each scan.

2.3.3. Mechanical Property Test

Based on GB/T50081-2019, the compressive strength was captured at the cycles of 0, 25, 50, 75, and 100 using The WAW1000 electro-hydraulic servo universal testing machine (Shanghai, China), as displayed in Figure 4. Furthermore, the loading rate for compressive strength was 0.5 MPa/s.

**Figure 4. The WAW1000** electro-hydraulic servo universal testing machine.

3. Results and Discussion

3.1. Macroscopic Mechanism Analysis

3.1.1. Analysis of GO on the Frost Resistance of the Ordinary SFRC

Mass Loss and Relative Dynamic Modulus of Elasticity with GO-SFRC

The mass loss of GO-SFRC concrete is shown in Figure 5a. It can be seen from Figure 5a that the mass loss of $G_{0.01}S_{25}$, $G_{0.03}S_{25}$, and ordinary SFRC concrete ($G_{0.00}S_{25}$) increases during the 50 freeze-thaw cycles, while the mass loss of $G_{0.05}S_{25}$ and $G_{0.07}S_{25}$ decreases.

Moreover, the slope (the ratio of mass loss to freeze-thaw cycles) of $G_{0.03}S_{25}$ concrete tends to be zero in the freeze-thaw process from 50 cycles to 75 cycles, which reveals the stable frost resistance of concrete to some extent. The mass loss of GO-SFRC concrete is higher than that of ordinary steel fiber concrete at the 25 freeze-thaw cycles. The reason may be that micro-cracks are formed on the contact surface because the bonding force between the steel fiber and the concrete is less than the frost heave force. However, the mass loss of all GO-SFRC specimens at the 100 cycles of freeze-thaw is less than that of ordinary SFRC.
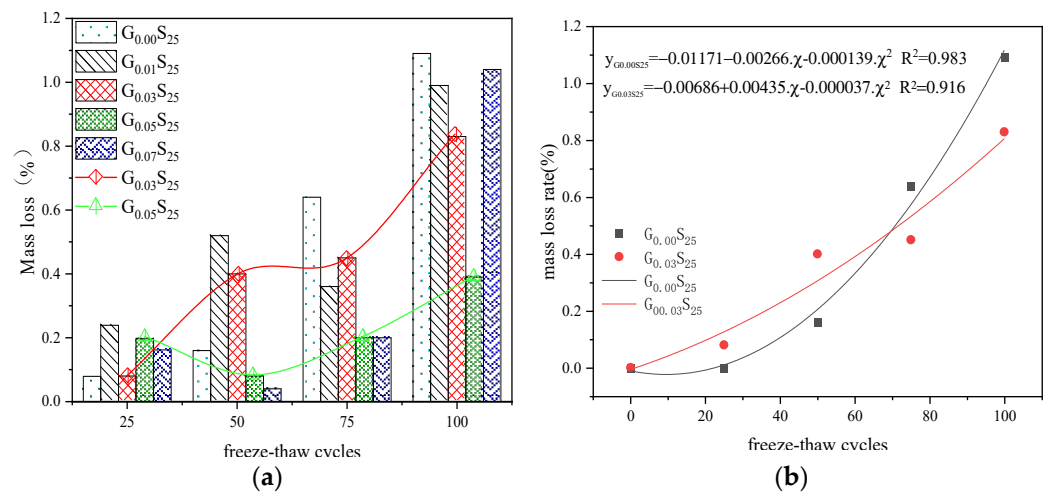
Figure 5. (**a**) GO-SFRC mass loss variation diagram; (**b**) $G_{0.00}S_{25}$, $G_{0.03}S_{25}$ curve fitting.

Figure 5b displays the discreteness of $G_{0.00}S_{25}$ and $G_{0.03}S_{25}$, which given out that the correlation coefficient R^2 of $G_{0.00}S_{25}$ and $G_{0.03}S_{25}$ was 0.916 and 0.983, respectively. The high reliability of the results provides some reference suggestions for further freeze-thaw tests and engineering applications of concrete.

Figure 6a presents the changes of the relative dynamic elastic modulus during different freeze-thaw cycles. It is observed that the other specimens are higher than $G_{0.00}S_{25}$, and they gradually decrease with the increase of freeze-thaw cycles. Before 50 freeze-thaw cycles, the relative dynamic elastic modulus of all the specimens except $G_{0.00}S_{25}$ is almost the same. While the curve of GO-SFRC decreases slowly in the 100 freeze-thaw cycles, compared with that of the ordinary SFRC concrete, which demonstrates that GO is effective in improving the frost resistance of SFRC concrete in the later stage. Figure 6b shows the correlation coefficient R^2 of $G_{0.00}S_{25}$ and $G_{0.03}S_{25}$ is 0.998 and 0.989, respectively, which indicates more minor error and higher reliability of test data.
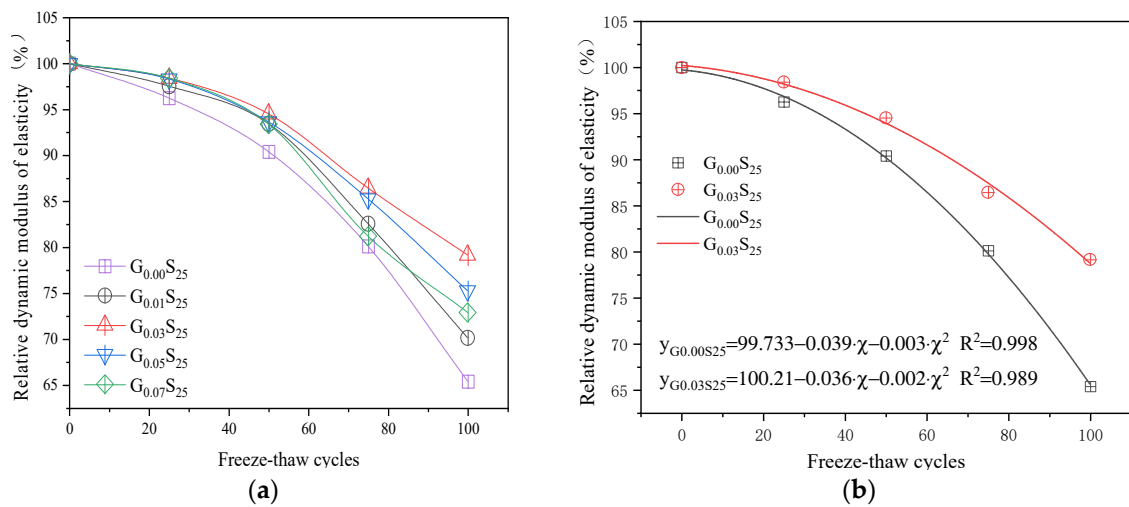
Figure 6. (**a**) GO-SFRC curve change diagram of relative dynamic elastic modulus; (**b**) $G_{0.00}S_{25}$, $G_{0.03}S_{25}$ curve fitting diagram of dynamic modulus and freeze-thaw times.

Mechanical Properties of GO-SFRC

Figure 7a and Table 10 show the variation of the compressive strength of SFRC concrete with different GO content. As can be seen from Figure 7a that the compressive strength of GO-SFRC concrete is higher than that of ordinary SFRC concrete in the same cyclic freeze-thaw process. The compressive strength of $G_{0.03}S_{25}$ increased by 22.39% at zero freeze-thaw cycle, compared with $G_{0.00}S_{25}$ (47.87 MPa). The strength loss of $G_{0.03}S_{25}$ was 22.14% at 100 freeze-thaw cycles. Its compressive strength is 47.78 MPa, which is approximately equal to the compressive strength of $G_{0.00}S_{25}$ (47.87 MPa) that is not affected by freeze-thaw cycles. The results show that GO can enhance the frost resistance of the SFRC concrete, for GO lamellar with interweaving and crosslinking serves as a template for hydration products to generate regular crystals and form dense microstructure [16–18,24]. This property of GO may play an important role in pervious concrete [35,36]. The regression analysis of Figure 7b presents a reasonable fitting degree of test data.
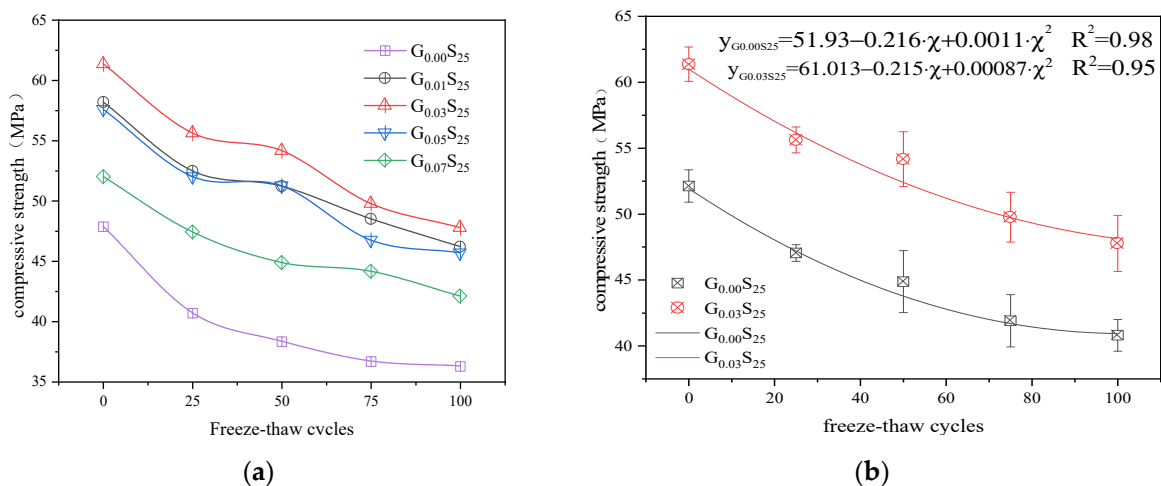

Figure 7. (**a**) GO-SFRC curve of compressive strength loss; (**b**) $G_{0.00}S_{25}$, $G_{0.03}S_{25}$ Fitting curve of compressive strength and number of freeze-thaw cycles.

Table 10. GO-SFRC compressive strength.

Go (%)	Compressive Strength Value after Freeze-Thaw Cycle (Mpa)				
	0 Times	25 Times	50 Times	75 Times	100 Times
$G_{0.00}S_{25}$	47.87	40.7	38.34	36.69	36.28
$G_{0.01}S_{25}$	58.2	52.48	51.21	48.51	46.2
$G_{0.03}S_{25}$	61.37	55.63	54.17	49.77	47.78
$G_{0.05}S_{25}$	57.6	52.01	51.25	46.73	45.68
$G_{0.07}S_{25}$	52	47.41	44.87	44.14	42.09

3.1.2. Analysis of GO-FA on the Frost Resistance of the Ordinary SFRC

Mass Loss of GO-FA-SFRC

Figure 8 shows the relationship between the mass loss of GO-FA-SFRC concrete and the dosage of FA. The mass loss of GO-FA-SFRC at the same GO content first decreased and then increased with the increase of FA content, such as $G_{0.03}F_{15}S_{25}$, $GO_{0.03}FA_{30}S_{25}$ and $G_{0.03}FA_{45}S_{25}$ at 100 freeze-thaw cycles. During the 50 freeze-thaw cycles, the mass loss of GO-FA-SFRC concrete was below 0.4%, and then it went up dramatically. During the 100 freeze-thaw cycles, the cumulative mass loss of GO-FA-SFRC concrete was lower than that of ordinary SFRC concrete, as displayed in Figure 8d. In a word, adding GO and FA to ordinary SFRC concrete can reduce the mass loss of concrete.
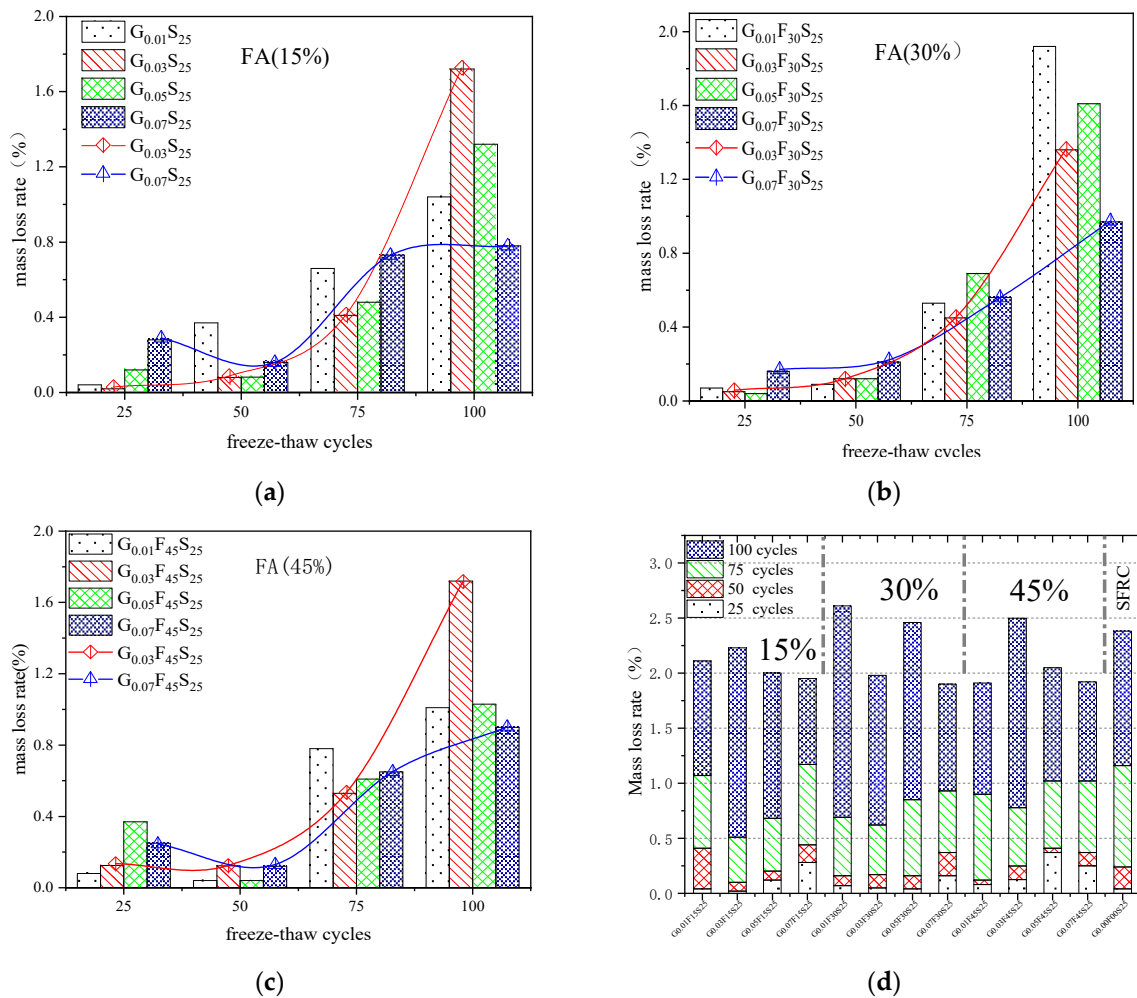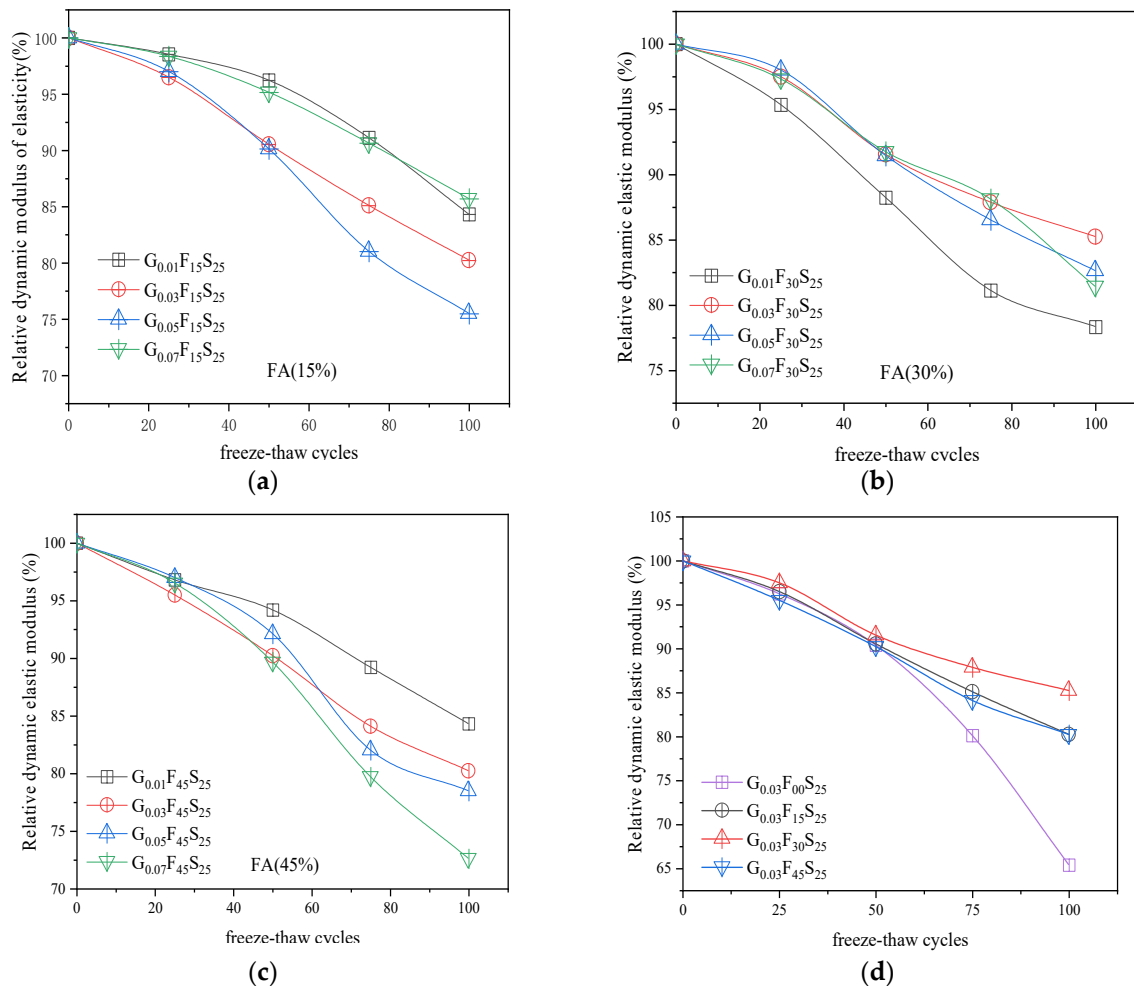

Figure 8. (**a**–**c**) Effect of FA-GO synergistic effect on quality loss of SFRC concrete; (**d**) The cumulative quality loss of GO-FA-SFRC concrete changes.

Relative Dynamic Elastic Modulus of GO-FA-SFRC

From Figure 9a–c, it can be seen that the relative dynamic elastic modulus of GO-FA-SFRC concrete with the same FA content decreases gradually as the number of freeze-thaw cycles increases. Combining with Figure 9d, it demonstrates that the relative dynamic elastic modulus of $G_{0.03}F_{30}S_{25}$ changes little, for GO with ultra-high elastic modulus and specific surface area is used as the crystal center to form a dense network, as well as the concrete pore is filled with FA particles in the hydration reaction. This reflects the synergistic effect of FA and GO. The synergistic effect of FA-GO can optimize the pore structure of SFRC concrete to a certain extent and improve the concrete compactness [27,29,37].


Figure 9. (**a**–**d**) Effect of FA-GO synergistic effect on relative dynamic modulus of SFRC concrete.

Mechanical Properties of GO-FA-SFRC

Table 11 and Figure 10 reveal the changes in the compressive strength of SFRC concrete with different dosages of GO-FA. From Figure 10a–c, it can be concluded that when the FA content is the same, the different content of FA makes the compressive strength of the GO-FA-SFRC concrete decrease with the increase of the number of freeze-thaw cycles. Figure 10d shows that the compressive strength curve of $G_{0.03}F_{30}S_{25}$ is significantly better than that of ordinary SFRC concrete during 100 freeze-thaw cycles, for FA is filled in the grid space formed by GO [31,33]. Combining the above mass loss and relative dynamic elastic modulus loss, it is concluded that $G_{0.03}F_{30}S_{25}$ with 0.03% GO and 30% FA owns the best frost resistance in this test.

Table 11. Change of compressive strength of GO-FA concrete.

Specimen Number	Compressive Strength Value After Freeze-Thaw Cycle (Mpa)				
	0 Times	25 Times	50 Times	75 Times	100 Times
$G_{0.01}F_{15}S_{25}$	41.73	38.25	37.05	34.58	32.94
$G_{0.03}F_{15}S_{25}$	41	37.13	35.39	33.53	32.55
$G_{0.05}F_{15}S_{25}$	40.97	36.18	33.54	32.06	31.92
$G_{0.07}F_{15}S_{25}$	44.19	39.39	39.13	35.49	34.22
$G_{0.01}F_{30}S_{25}$	45.53	43.02	38.25	36.48	34.99
$G_{0.03}F_{30}S_{25}$	46.11	43.27	40.2	38.7	36.8
$G_{0..05}F_{30}S_{25}$	46.67	43.92	41.66	39.08	35.45
$G_{0.07}F_{30}S_{25}$	44.8	41.59	39.91	37.11	34.84
$G_{0.01}F_{45}S_{25}$	45.97	45.72	44.37	37.38	35.63
$G_{0.03}F_{45}S_{25}$	43.63	43.3	43.7	36.48	34.27
$G_{0.05}F_{45}S_{25}$	40.63	40.4	40.66	35.93	34.16
$G_{0.07}F_{45}S_{25}$	39.4	38.98	38.17	34.65	32.59
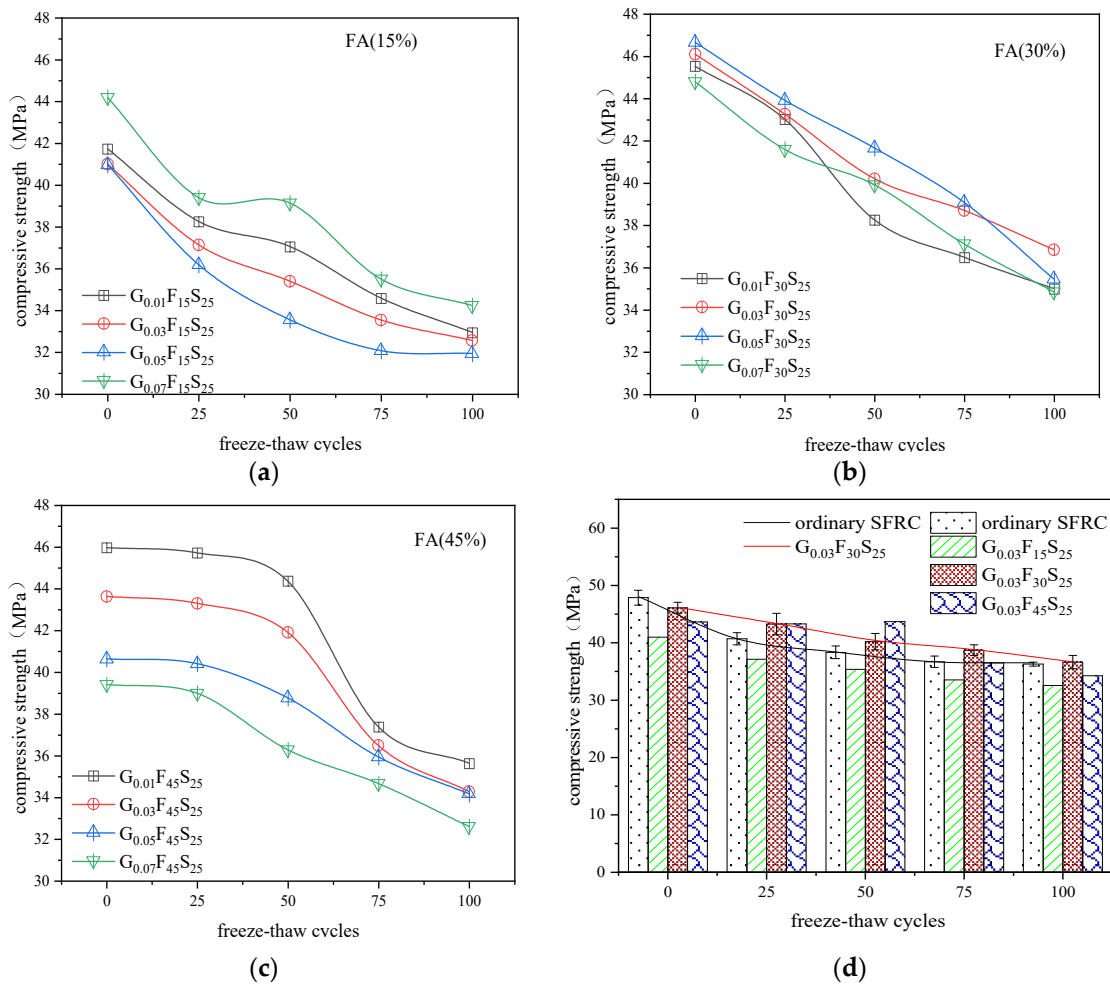
**Figure 10.** (**a**–**d**) Strength loss curve of GO-FA-SFRC concrete.

3.2. Microscopic Mechanism Analysis

3.2.1. Distribution of the Microscopic Pore Structure of GO-SFRC

In order to deeply discuss the frost resistance of GO-SFRC concrete from a microscopic point, five samples were selected for CT scanning, including $G_{0.00}S_{25}$, $G_{0.01}S_{25}$, $G_{0.03}S_{25}$, $G_{0.05}S_{25}$, and $G_{0.07}S_{25}$, respectively.

Figure 11 visually shows the changes in the internal pores of the concrete after GO is added to the SFRC concrete. The pore morphology characteristics develop from pie-shaped,

long columnar to cobblestone, ellipsoidal, and nearly spherical, which is conducive to frost resistance, as presented in Figure 11.
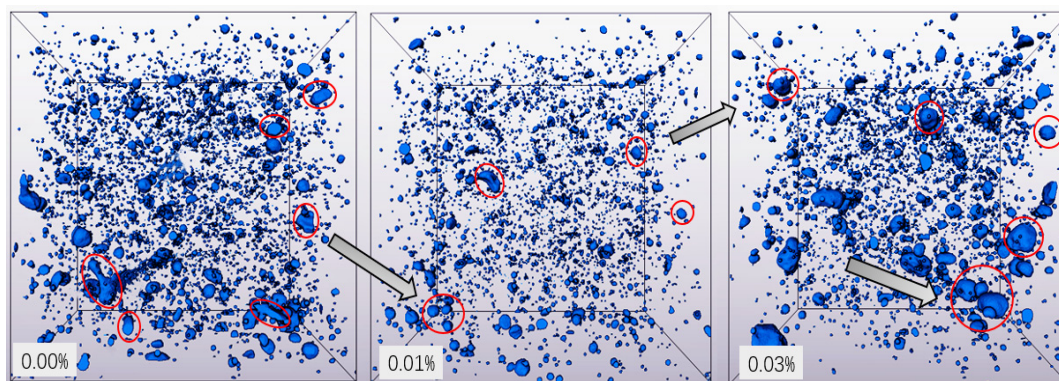

Figure 11. Characterization of pore morphology by graphene oxide effect.

Figure 12 and Table 12 visually reveal the changes of the internal pore morphology of the specimens with the GO admixture in the range of 0.01–0.07%. From Figure 12e,d,j, the distribution and size of the pores inside the concrete can be visually observed. With the increase of GO content, the pore space position gradually develops from scattered and uneven distribution to a more uniform and reasonable spatial position distribution, which reduces the stress concentration and improves the compressive strength of concrete on a macro level;

Table 12. Internal pore parameters of GO-SFRC structure.

Go (%)	Number of Holes	Porosity (%)
$G_{0.00}S_{25}$	41,074	0.914
$G_{0.01}S_{25}$	22,378	0.828
$G_{0.03}S_{25}$	13,342	0.729
$G_{0.05}S_{25}$	16,321	0.937
$G_{0.07}S_{25}$	57,131	1.026

According to Table 12, the total number of pores is far less than that of pores in $G_{0.00}S_{25}$, which decreases about 67.52%. As well, $G_{0.03}S_{25}$ drops to 0.729%, which is a decrease of 0.185%. Therefore, the addition of GO can reduce the number and of pores and the average porosity and enhance the compactness of concrete [24,28]. The properties of graphene oxide will play an important role in the research of green concrete [37–46].
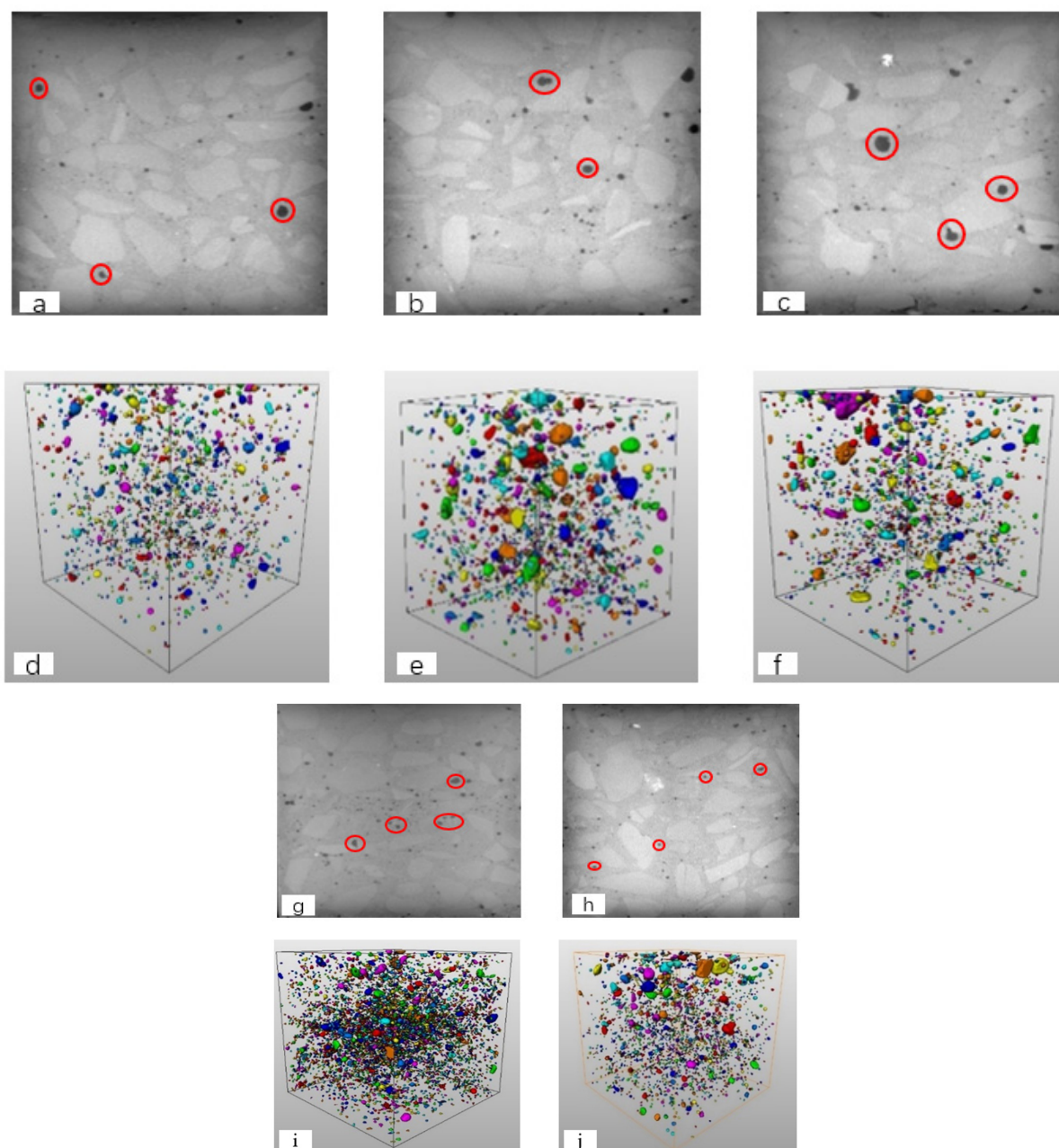
Figure 12. Internal pore structure and distribution of GO-SFRC. (**a**) G0.01S25 of 2D. (**b**) G0.03S25 of 2D. (**c**) G0.05S25 of 2D. (**d**) G0.01S25 of 3D. (**e**) G0.03S25 of 3D. (**f**) G0.05S25 of 3D. (**g**) G0.07S25 of 2D. (**h**) G0.00S25 of 2D. (**i**) G0.07S25 of 3D. (**j**) G0.00S25 of 3D.

### 3.2.2. Distribution of the Microscopic Pore Structure of GO-FA-SFRC

Aiming at discussing the effect of the different amounts of FA on GO-FA-SFRC concrete, the $G_{0.03}F_{15}S_{25}$, $G_{0.03}F_{30}S_{25}$, and $G_{0.03}F_{45}S_{25}$ are extracted from the specimens for CT scan. It is verified that adding the same amount of GO to the steel fiber concrete can optimize the particle gradation, and the particles of different sizes can give full play to the filling effect and produce a synergistic effect, thereby improving the density of the steel fiber concrete, as shown in Figure 13.
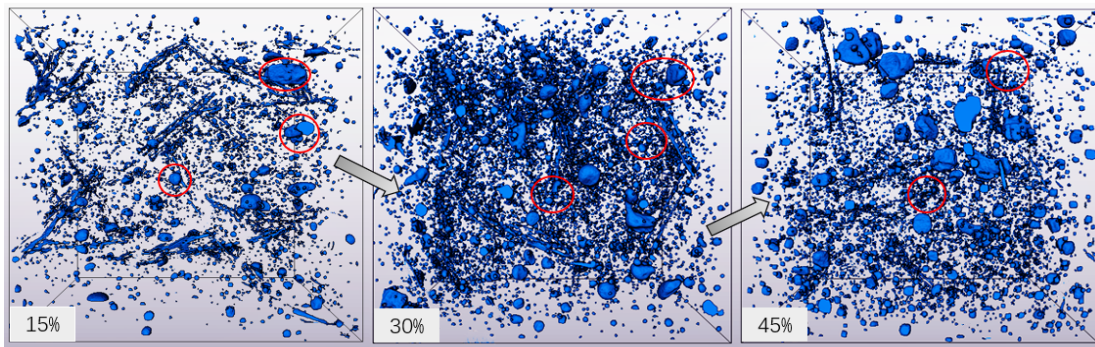
Figure 13. Gradation effect of fly ash and graphene oxide.

Figure 14 and Table 13 demonstrate the pore morphology distribution in the concrete after freezing and thawing. From Figure 14, we can directly observe the improvement of 0.03% GO and different amounts of FA on the concrete pores. Figure 14a,d shows the pore morphology of $G_{0.03}F_{15}S_{25}$ in 2D and $G_{0.03}F_{15}S_{25}$ in 3D, most of which are ellipsoidal, nearly spherical, and biscuit-shaped. The number of pores at this dosage is 22,345, and the average porosity is 0.915%; with the increase of FA content, the number of pores in $G_{0.03}F_{30}S_{25}$ increased by 39,838. It is worth noting that the average porosity decreased by 0.821%. The reason may be that FA filled the large pores and split them, making them harmless (Figure 13). As a result, the number of delicate pores has increased dramatically. The results display that the addition of GO-FA to ordinary SFRC concrete can systematically optimize the pores, and FA particles of different sizes can give full play to the filling effect, offering an excellent synergistic effect; when the content from $G_{0.03}FA_{30}S_{25}$ to $G_{0.03}FA_{45}S_{25}$, the average porosity of SFRC concrete continued to crease to 0.886%.
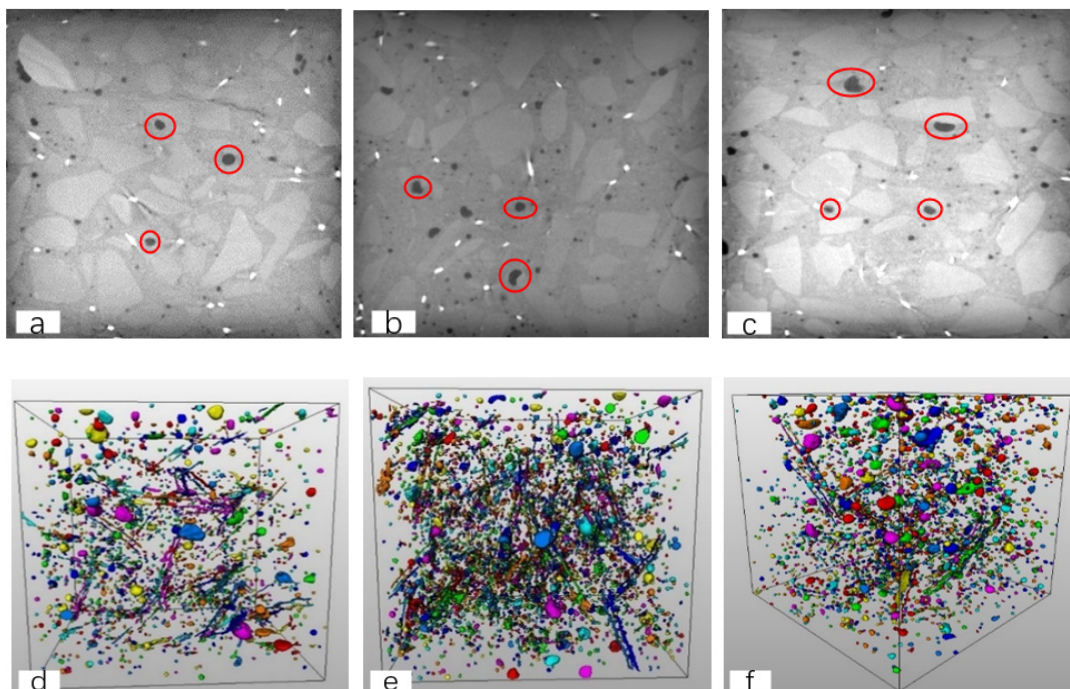
Figure 14. Internal pore structure and morphology distribution of GO-FA. (**a**) G0.03F15S25 of 2D. (**b**) G0.03F30S25 of 2D. (**c**) G0.03F45S25 of 2D. (**d**) G0.03F15S25 of 3D. (**e**) G0.03F30S25 of 3D. (**f**) G0.03F45S25 of 3D.

Table 13. Internal pore parameters of GO-SFRC structure.

Fa(%)	Number of Holes	Porosity (%)
$G_{0.03}F_{15}S_{25}$	22,345	0.915
$G_{0.03}F_{30}S_{25}$	39,838	0.821
$G_{0.03}F_{45}S_{25}$	38,126	0.886

3.3. Pore Size Distribution

3.3.1. Pore Distribution of GO-SFRC

Figure 15 shows the pore quantity distribution of GO-SFRC concrete. It reveals that the proportions of different pore volumes also change with the GO content changes. Combined with Figure 15 and Table 14, it can be concluded that the pore proportion of 0.01–0.05 mm^3, 0.05–0.1 mm^3, 0.1–0.5 mm^3 and 0.5–1 mm^3 first increases and then decreases with the increase of GO content, which reaches the peak value at $G_{0.03}S_{25}$ compared with ordinary SFRC concrete. The results demonstrate that the GO can change the microstructure of SFRC concrete. Combined with the fact that the pore number of (the $G_{0.03}S_{25}$) and the average porosity with the dosage of 0.03% GO above are both minimum values, which indicates that the addition of GO into SFRC concrete can make the connected holes turn into closed holes [34].
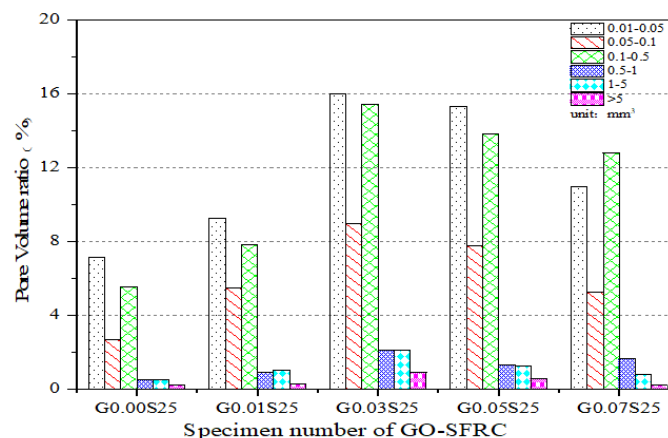
Figure 15. Pore distribution in GO–SFRC.

Table 14. Pore volume ratios of different scales inside GO-SFRC unit: mm^3.

GO (%)	Pore Volume (%)						
	$V \leq 0.01$	$0.01 < V \leq 0.05$	$0.05 < V \leq 0.1$	$0.1 < V \leq 0.5$	$0.5 < V \leq 1$	$1 < V \leq 5$	$V > 5$
$G_{0.00}S_{25}$	83.44	7.13	2.65	5.54	0.53	0.48	0.23
$G_{0.01}S_{25}$	75.22	9.27	5.51	7.81	0.91	1.01	0.27
$G_{0.03}S_{25}$	54.43	16.02	8.96	15.46	2.1	2.11	0.91
$G_{0.05}S_{25}$	59.9	15.32	7.79	13.82	1.33	1.28	0.57
$G_{0.07}S_{25}$	68.33	10.96	5.25	12.8	1.63	0.82	0.2

3.3.2. Pore Distribution of GO-FA-SFRC

Figure 16 and Table 15 display the pores size distribution of GO-FA-SFRC at the different ratios of FA. It can be seen that the pore ratio of less than 0.01 mm^3 increases correspondingly, while the pore ratio of greater than 5 mm^3 decreases continuously with the increase of FA content. Combined with the freezing resistance evaluation of $G_{0.03}F_{30}S_{25}$ above, the freezing resistance of concrete at this time is better than that of ordinary SFRC. Meanwhile, the result also indicates that FA particles can fill large holes and split them into tiny holes in this passage.
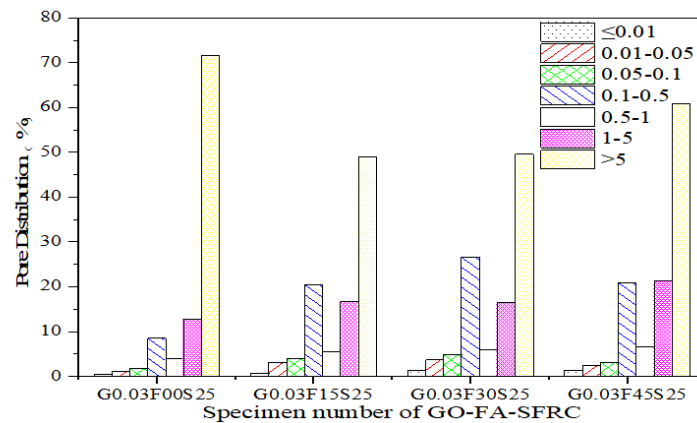
Figure 16. The Pore distribution in GO–FA–SFRC.

Table 15. GO-FA-SFRC internal pore quantity distribution unit: mm³.

FA (%)	The Pore Number (%)						
	$V \leq 0.01$	$0.01 < V \leq 0.05$	$0.05 < V \leq 0.1$	$0.1 < V \leq 0.5$	$0.5 < V \leq 1$	$1 < V \leq 5$	$V \geq 5$
$G_{0.00}F_{00}S_{25}$	54.43	16.02	8.96	15.46	2.1	2.11	0.91
$G_{0.03}F_{15}S_{25}$	66.29	14.29	6.14	11.11	0.89	0.93	0.36
$G_{0.03}F_{30}S_{25}$	59.88	16.78	7.56	13.61	0.98	0.86	0.33
$G_{0.03}F_{45}S_{25}$	71.16	11.15	4.84	10.47	1.02	1.05	0.31

4. Conclusions

Based on the freeze-thaw cycle test, this paper studies the synergistic effect of GO and FA on the durability of the SFRC and its improvement mechanism. The main conclusions are as follows.

(1) The addition of GO and FA to SFRC has different degrees of improvement on the frost resistance. According to the analysis of compressive strength loss, relative dynamic elastic modulus and mass loss, it is determined that frost resistance of GO-FA-SFRC is the best when the GO content is 0.03% and the FA content is 30%.

(2) The frost resistance indexes of GO-SFRC are better than ordinary steel fiber concrete. Compared with SFRC, the pore distribution of GO-SFRC is more uniform, and the pore shape of GO-SFRC is similar to the spherical and ellipsoidal closed pore. This pore shape has a significant effect in improving the frost resistance of concrete.

(3) Since GO has a powerful regulatory effect, the pore morphology of GO-SFRC is spherical and ellipsoidal by adding 0.03% GO. Furthermore, the addition of 30% FA makes the large volume pores of GO-SFRC become tiny volume pores so that GO-FA-SFRC presents better frost resistance.

Author Contributions: Methodology and investigation, X.Y.; data curation and writing—original draft preparation, M.D., S.Z. and M.Z.; writing—review and editing, M.L.; supervision, M.L. All authors have read and agreed to the published version of the manuscript.

Conflicts of Interest: The authors declare no conflict of interest.

References

1. Sanchez, F.; Sobolev, K. Nanotechnology in concrete—A review. *Constr. Build. Mater.* **2010**, *24*, 2060–2071. [CrossRef]
2. Li, W.; Ji, W.; Forood-Torabian, I.; Wang, Y.; Li, G.; Liu, Y.; Xing, F. Nano-Silica Sol-Gel and Carbon Nanotube Coupling Effect on the Performance of Cement-Based Materials. *Nanomaterials* **2017**, *7*, 185. [CrossRef]
3. Zhou, G.X.; Li, C.; Zhao, Z.; Qi, Y.Z.; Yang, Z.H.; Jia, D.C.; Zhong, J.; Zhou, Y. 3D printing geopolymer nanocomposites: Graphene oxide size effects on a reactive matrix. *Carbon* **2020**, *164*, 215–223. [CrossRef]
4. Wang, L.; Zheng, D.; Zhang, S.; Cui, H.; Li, D. Effect of Nano-SiO$_2$ on the Hydration and Microstructure of Portland Cement. *Nanomaterials* **2016**, *6*, 241. [CrossRef]
5. Yoo, D.Y.; Kim, S.; Park, G.J.; Park, J.J.; Kim, S.W. Effects of fiber shape, aspect ratio, and volume fraction on flexural behavior of ultra-high-performance fiber-reinforced cement composites. *Compos. Struct.* **2017**, *174*, 375–388. [CrossRef]
6. Alrekabi, S.; Cundy, A.B.; Lampropoulos, A.; Whitby, R.L.D.; Savina, I. Mechanical performance of novel cement-based composites prepared with nano-fibres, and hybrid nano- and micro-fibers. *Compos. Struct.* **2017**, *178*, 145–156. [CrossRef]
7. Qureshi, T.S.; Panesar, D.K. Impact of graphene oxide and highly reduced graphene oxide on cement based composites. *Constr. Build. Mater.* **2015**, *206*, 71–83. [CrossRef]
8. Zhao, Y.; Liu, Y.; Shi, T.; Gu, Y.; Zheng, B.; Zhang, K.; Xu, J.; Fu, Y.; Shi, S. Study of mechanical properties and early-stage deformation properties of graphene-modified cement-based materials. *Constr. Build. Mater.* **2020**, *257*, 119498. [CrossRef]
9. Yao, X.; Shamsaei, E.; Chen, S.; Zhang, Q.H.; de Souza, F.B.; Sagoe-Crentsil, K.; Duan, W. Graphene oxide-coated Poly(vinyl alcohol) fibers for enhanced fiber-reinforced cementitious composites. *Compos. Part B Eng.* **2019**, *174*, 107010. [CrossRef]
10. Yao, X.; Shamsaei, E.; Wang, W.; Zhang, S.; Sagoe-Crentsil, K.; Duan, W. Graphene-based modification on the interface in fibre reinforced cementitious composites for improving both strength and toughness. *Carbon* **2020**, *170*, 493–502. [CrossRef]
11. Ahmed, H.U.; Faraj, R.H.; Hilal, N.; Mohammed, A.A.; Sherwani, A.F.H. Use of recycled fibers in concrete composites: A systematic comprehensive review. *Compos. Part B Eng.* **2021**, *215*, 108769. [CrossRef]
12. Uygunoğlu, T.; Şimşek, B.; Ceran, Ö.B.; Eryeşil, Ö. Novel hybrid fiber reinforced mortar production using polyvinyl alcohol with a blend of graphene oxide and silver nanoparticles. *J. Build. Eng.* **2021**, *44*, 102641. [CrossRef]
13. Wilson, N.R.; Pandey, P.A.; Beanland, R.; Young, R.J.; Kinloch, I.A.; Gong, L.; Liu, Z.; Suenaga, K.; Rourke, J.P.; York, S.J. Graphene oxide: Structural analysis and application as a highly transparent support for electron microscopy. *ACS Nano* **2009**, *3*, 2547–2556. [CrossRef]
14. Shamsaei, E.; de Souza, F.B.; Yao, X.; Benhelal, E.; Akbari, A.; Duan, W. Graphene-based nanosheets for stronger and more durable concrete: A review. *Constr. Build. Mater.* **2018**, *183*, 642–660. [CrossRef]
15. Zhou, Y.; Xiong, C.; Peng, Z.; Huang, J.; Chang, H. Molecular dynamics simulation of the interfacial interaction mechanism between functional groups on graphene-based two-dimensional matrix and calcium silicate hydrate. *Constr. Build. Mater.* **2021**, *284*, 122804. [CrossRef]
16. Lu, S.; Luo, X.; Zhang, J. Graphere oxide controlled cement materials formation of large-scale ordered structure and its properties characterization. *Mater. Rep.* **2017**, *31*, 10–14. (In Chinese)
17. Yujie, F.; Jianping, Z.; Li, W. Effect of graphene oxide on compressive strength and microstructure of slag cement. *J. Henan Polytech. Univ.* **2021**, *40*, 169–175. (In Chinese)
18. Shenghua, L.; Li, S.; Jia, Z. High/Ultra-high performance graphene oxide/cement-based composites with large-scale, ordered and compact flower-like microstructures. *Mater. Rep.* **2017**, *31*, 78–84. (In Chinese)
19. Lu, L.; Ouyang, D. Properties of Cement Mortar and Ultra-High Strength Concrete Incorporating Graphene Oxide Nanosheets. *Nanomaterials* **2017**, *7*, 187. [CrossRef]
20. Wan, H.; Zhang, Y. Interfacial bonding between graphene oxide and calcium silicate hydrate gel of ultra-high performance concrete. *Mater. Struct.* **2020**, *53*, 34. [CrossRef]
21. Szeląg, M. Mechano-Physical Properties and Microstructure of Carbon Nanotube Reinforced Cement Paste after Thermal Load. *Nanomaterials* **2017**, *7*, 267. [CrossRef]
22. Rehman, S.K.U.; Ibrahim, Z.; Memon, S.A.; Aunkor, T.H.; Javed, M.F.; Mehmood, K.; Shah, S.M.A. Influence of Graphene Nanosheets on Rheology, Microstructure, Strength Development and Self-Sensing Properties of Cement Based Composites. *Sustainability* **2018**, *10*, 822. [CrossRef]
23. Yang, H.; Cui, H.; Tang, W.; Li, Z.; Han, N.; Xing, F. A critical review on research progress of graphene/cement based composites. *Compos. Part A Appl. Sci. Manuf.* **2017**, *102*, 273–296. [CrossRef]
24. Xixi, S.; Guangjun, S. Effect of graphene oxide on mechanical properties of cement based materials. *Non-Met. Mines* **2021**, *44*, 47–50. (In Chinese)
25. Tong, T.; Fan, Z.; Liu, Q.; Wang, S.; Tan, S.; Yu, Q. Investigation of the effects of graphene and graphene oxide nanoplatelets on the micro- and macro-properties of cementitious materials. *Constr. Build. Mater.* **2016**, *106*, 102–114. [CrossRef]
26. Mohammed, A.; Sanjayan, J.G.; Duan, W.H.; Nazari, A. Incorporating graphene oxide in cement composites: A study of transport properties. *Constr. Build. Mater.* **2015**, *84*, 341–347. [CrossRef]
27. Chuah, S.; Pan, Z.; Sanjayan, J.G.; Wang, C.M.; Duan, W.H. Nano reinforced cement and concrete composites and new perspective from graphene oxide. *Constr. Build. Mater.* **2014**, *73*, 113–124. [CrossRef]
28. Kai, M.F.; Zhang, L.W.; Liew, K.M. Graphene and graphene oxide in calcium silicate hydrates: Chemical reactions, mechanical behavior and interfacial sliding. *Carbon* **2019**, *146*, 181–193. [CrossRef]

29. Wang, G.; Liu, L.; Zhang, Z. Interface mechanics in carbon nanomaterials-based nanocomposites. *Compos. Part A Appl. Sci. Manuf.* **2021**, *141*, 106212. [CrossRef]

30. Pan, Z.; He, L.; Qiu, L.; Korayem, A.H.; Li, G.; Zhu, J.W.; Collins, F.; Li, D.; Duan, W.H.; Wang, M.C. Mechanical properties and microstructure of a graphene oxide-cement composite. *Cem. Concr. Compos.* **2015**, *58*, 140–147. [CrossRef]

31. Meiyan, H.; Zhongke, S.; Yanmei, G. Effect of fly ash on property and microstructure of UHPC. *China Concr. Cem. Prod.* **2020**, *11*, 14–19. (In Chinese)

32. Qianyun, W.; Qinyong, M.; Ying, W. Compression-tensile tests and meso-structure of basalt fiber-slag powder-fly ash concrete under freeze-thaw cycles. *Acta Mater. Compos. Sin.* **2021**, *38*, 953–965. (In Chinese)

33. Jianwu, Z.; Xiao, W.; Zhixin, L. Influence and mechanism of GO on the property of high content fly ash cement-based material. *New Chem. Mater.* **2021**, *49*, 240–243. (In Chinese)

34. Dongpo, L.; Cang, D. Study on freeze-thaw damage mechanical properties of cement-based materials based on the synergistic effect of slag powder and graphene oxide. *Chin. J. Appl. Mech.* **2021**, *38*, 1431–1440. (In Chinese)

35. Xiaosa, Y.; Baomin, W.; Peng, C.; Tao, L. Study on the Frost Resistance of Concrete Modified with Steel Balls Containing Phase Change Material (PCM). *Materials* **2021**, *14*, 4497.

36. Li, L.G.; Feng, J.J.; Lu, Z.C.; Xie, H.Z.; Xiao, B.F.; Kwan, A.K.H. Effects of aggregate bulking and film thicknesses on water permeability and strength of pervious concrete. *Powder Technol.* **2022**, *396*, 743–753. [CrossRef]

37. Devi, S.C.; Khan, R.A. Effect of graphene oxide on mechanical and durability performance of concrete. *J. Build. Eng.* **2020**, *27*, 101007. [CrossRef]

38. Herath, C.; Gunasekara, C.; Law, D.W.; Setunge, S. Performance of high volume fly ash concrete incorporating additives: A systematic literature review. *Constr. Build. Mater.* **2020**, *258*, 120606. [CrossRef]

39. Sun, J.; Ma, Y.; Li, J.; Zhang, J.; Ren, Z.; Wang, X. Machine learning-aided design and prediction of cementitious composites containing graphite and slag powder. *J. Build. Eng.* **2021**, *43*, 102544. [CrossRef]

40. Sun, J.; Wang, J.; Zhu, Z.; He, R.; Peng, C.; Zhang, C.; Wang, X. Mechanical Performance Prediction for Sustainable High-Strength Concrete Using Bio-Inspired Neural Network. *Buildings* **2022**, *12*, 65. [CrossRef]

41. Sun, J.; Lin, S.; Zhang, G.; Sun, Y.; Zhang, J.; Chen, C.; Wang, X. The effect of graphite and slag on electrical and mechanical properties of electrically conductive cementitious composites. *Constr. Build. Mater.* **2021**, *281*, 122606. [CrossRef]

42. Sun, J.; Tang, Y.; Wang, J.; Wang, X.; Wang, J.; Yu, Z.; Wang, Y. A multi-objective optimisation approach for activity excitation of waste glass mortar. *J. Mater. Res. Technol.* **2022**, *17*, 2280–2304. [CrossRef]

43. Tang, Y.; Feng, W.; Chen, Z.; Nong, Y.; Guan, S.; Sun, J. Fracture behavior of a sustainable material: Recycled concrete with waste crumb rubber subjected to elevated temperatures. *J. Clean. Prod.* **2021**, *318*, 128553. [CrossRef]

44. Sun, J.; Aslani, F.; Lu, J.; Wang, L.; Huang, Y.; Ma, G. Fibre-reinforced lightweight engineered cementitious composites for 3D concrete printing. *Ceram. Int.* **2021**, *47*, 27107–27121. [CrossRef]

45. Yang, Y.; Chen, Z.; Feng, W.; Nong, Y.; Yao, M.; Tang, Y. Shrinkage compensation design and mechanism of geopolymer pastes. *Constr. Build. Mater.* **2021**, *299*, 123916. [CrossRef]

46. Sun, J.; Wang, Y.; Liu, S.; Dehghani, A.; Xiang, X.; Wei, J.; Wang, X. Mechanical, chemical and hydrothermal activation for waste glass reinforced cement. *Constr. Build. Mater.* **2021**, *301*, 124361. [CrossRef]